



Linear Stability Analyses of HIFiRE-1 and ROTEX-T in Mach 6 cruise

Vojtech Pezlar, Anton Burtsev, Vassilis Theofilis³

Abstract

Local and global stability analyses and direct numerical simulations are performed to study unresolved questions on laminar-turbulent transition mechanisms that condition performance of the HIFiRE-1 and ROTEX-T flight vehicles at hypersonic flight conditions. Conditions at which the Mack mode is stable on the conical forebodies preceding the compression (on the ROTEX-T) and expansion (on the HIFiRE-1) regions on the vehicles are identified and the BiGlobal eigenvalue problem in these regions is solved under physically admissible homogeneous Dirichlet inflow boundary conditions. The global eigenmodes responsible for unsteadiness on the flare of the two vehicles are then identified, alongside several stationary and traveling members of the global eigenspectra. Axisymmetric direct numerical simulations provide evidence of linear destabilization of the flow on the ROTEX-T vehicle as the Reynolds number is systematically increased. Three-dimensional direct numerical simulations of a quarter- and the full ROTEX-T vehicle, both at zero angle of attack, have produced identical unsteady flowfields, a result which points at the unsteadiness on the vehicle arising from linear global instability originating at the reattachment zone of the laminar separation bubble formed at the flare.

Keywords: ROTEX-T, HIFiRE-1, Linear Global Flow Stability, Direct Numerical Simulation

Nomenclature

Latin

 $m\,$ – Azimuthal wavenumber

p - Pressure, Pa u - Velocity, m/s

 q_w – Wall heat flux, W·m⁻²

x – Distance along centerline, m

y - Centerline-normal distance, m

F - Frequency, Hz

 L_c – Cone length, m

 $M\,$ – Mach number

 Re_{L_c} – Cone length L_c based Reynolds number

St - Modified Stanton number

T – Temperature, K

Greek

 α - Complex wavenumber

 β – Spanwise wavenumber

 η – Wall-normal distance, m

 μ – Dynamic viscosity, Pa · s

 ω – Complex frequency

 ϕ – LE Shock angle, °

 ρ – Density, kg/m³

au – Shear stress, Pa

 θ – Cone half-angle, °

 ξ – Distance along cone surface, m

Subscripts

0 – Stagnation

 ∞ - Freestream

e - Boundary-layer edge

n – Nose

w - Wall

¹Technion - Israel Institute of Technology, Haifa, IL, vojtech-p@campus.technion.ac.il

²The University of Texas at Austin, Austin, TX, anton.burtsev@austin.utexas.edu

³Technion - Israel Institute of Technology, Haifa, IL, vassilis@technion.ac.il

1. Introduction

Schmisseur [1] discussed the Hypersonic International Flight Research Experiment (HIFiRE) series of research vehicles, which was conceived by the US Air Force as a sequence of platforms on which a systematic increase of geometric vehicle complexity would lead to the introduction of ever more complex physical mechanisms of boundary layer laminar-turbulent transition, so that coordinated ground experimentation, numerical simulation, and flight testing could address different paths to transition in isolation. HIFiRE-1 [2] featured a cone, on which classic Mack mode instabilities were expected to develop, followed by a cylinder and a flare, where the nominally axisymmetric separation bubble formed under the compression shock could become transitional. The Rocket Technology Flight Experiment-Transition (ROTEX-T) was introduced by DLR [3] as a complementary configuration, on which the cone is followed by a flare and then a cylinder, which potentially advances transition to a location closer to the cone than on the HIFiRE-1. While work on the HIFiRE-1 has somewhat subsided, and now continues on the more recent HIFLIER configuration [4], vigorous research on the ROTEX-T is still underway, mostly comparing results of ground experiments and simulations [e.g. 5, 6] with those of the flight experiment at a relatively wide range of free stream flow conditions. Other research vehicles in the HIFiRE series were also discussed by Schmisseur [1], most notably the HIFiRE-5 flight vehicle, having the shape of an elliptic cone, on which three-dimensional boundary layer instability and transition phenomena could be studied in flight [e.g. 7] and ground experiments [e.g. 7, 8], as well as accompanying theoretical [e.g. 9-11] and simulation [12] work.

The present contribution returns to the question of linear instability mechanisms of different physical origin appearing at typical locations on the Cone-Cylinder-Flare (CCF) and Cone-Flare-Cylinder (CFC) model geometries, respectively representing the HIFIRE-1 and ROTEX-T vehicles. In addition, qualitative differences between the CFD and the Cone-Flare (CF) model of the ROTEX-T, the latter also used in experiments as a ROTEX-T model, are addressed. Tools applied include compressible boundary layer theory and spatial local linear stability theory for the conical part of the geometries, unsteady laminar axisymmetric direct numerical simulation for the computation of steady axisymmetric base flows at parameters at which such states exist, followed by modal and/or nonmodal BiGlobal linear stability analysis at spatially inhomogeneous regions of the flow, namely cone-cylinder and cylinder-flare on the HIFIRE-1 and cone-flare on the ROTEX-T and, finally, full three-dimensional direct numerical simulations of the respective vehicle configurations. Both configurations feature a 7° half angle (though different nose radii have been considered), while all analyses and simulations were performed at the same free-stream Mach number $M_{\infty}=6$.

2. Laminar axisymmetric base flows

2.1. Definition of the HIFiRE-1 and ROTEX-T vehicles

In a first step aiming to make the conical sections of the two vehicles identical, while matching the ROTEX-T geometry on which recent experiments and analyses have been performed [5], the HIFiRE-1 was scaled by 37% and the ROTEX-T by 39%, see Figure 1. The flow Reynolds number is built with the length of the cone up to the cone-flare junction on the ROTEX-T / cone-cylinder shoulder on the HIFiRE-1, i.e. the length L_c between the cone nose and the projection of the point denoted S4 on Fig. 1 on the axis of symmetry. The abscissae of the points indicated on this figure, which will be referred to in the analyses that follow, are S1: x=0.25 m, S2: x=0.30 m, S3: x=0.36 m and S4: x=0.406 m. The remaining geometric and flow parameters are summarized in Table 1).

Table 1. Vehicle geometries and conditions analyzed at $M_{\infty}=6$

Configuration	Case	Lc [mm]	$Re \times 10^{-3}$	r_n [mm]	T_0 [K]	T_{∞} [K]	T_w [K]
HIFiRE-1	37% scale	406.6	500	0.99	550	67.07	290
ROTEX-T	39% scale	406.6	500 – 2,000	0.99	550	67.07	290
	Flight	1040.8	1,000	2.5	1279	238.075	330

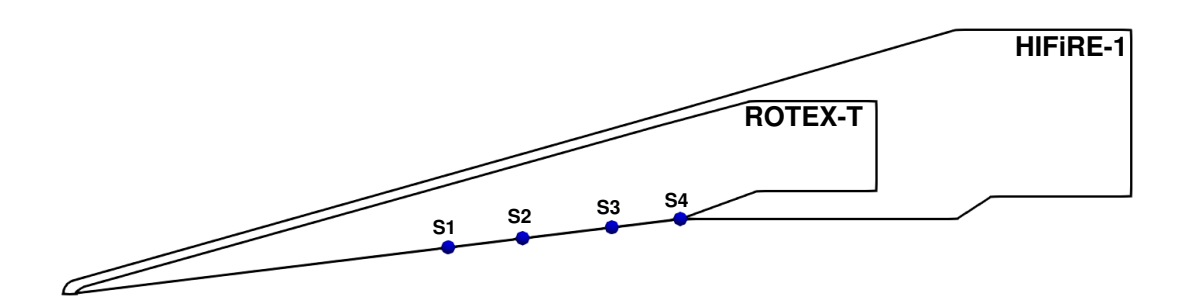


Fig 1. Schematic comparison of the resolved flow fields around the scaled ROTEX-T and HIFiRE-1 geometries.

2.2. Axisymmetric laminar steady flows

Steady flows $\bar{q}=(\bar{\rho},\bar{u}_1,\bar{u}_2,\bar{u}_3,\bar{T})^{\mathsf{T}}$, used in the subsequent linear local and global stability analyses have been obtained by unsteady laminar computations without a turbulence model using OpenFOAM. Resolutions employed featured in excess of 10 million cells, comparable to those used in our recent related (SU2) work with the CF model of the ROTEX-T geometry [5]. Rather small time-steps required by these meshes, combined with the level of convergence shown in results that follow, have resulted in computational cost comparable or higher to that of the steady simulations performed in [5]. Qualitative features of the respective flow fields are shown as numerical Schlieren images in Figure 2. At the point where the cone terminates on the two configurations the main difference arises from the separation bubble formed on the ROTEX-T on account of flow compression at the flare. This is of course absent on the HIFiRE-1, where flow expansion leads to attached flow up to the shoulder. This and other flow features will be further discussed and quantified in what follows.



Fig 2. Qualitative features of the steady flows formed on the scaled ROTEX-T (upper image) and HIFiRE-1 (lower image) geometries at $M_{\infty}=6, Re=5\times10^5$

2.3. CF vs CFC geometries

An aspect differentiating the present from earlier related work on the ROTEX-T is the present use of the cone-flare-cylinder (CFC) geometry, as opposed to the cone-flare (CF) configuration used in earlier work [5]. In Figure 3, features of the flows obtained by unsteady axisymmetric simulations are highlighted in the neighborhood of the respective flares. While the separation shock characteristics are analogous, two major differences are immediately visible, namely the absence of the expansion on the CF geometry alongside the difference in the extent of the laminar separation bubbles forming at the flare. Another aspect not visible in the image but clearly seen in the simulation results is unsteadiness of the flowfield above the (relatively long) flare of the CF geometry, a feature altogether absent on the CFC configuration. In what follows, the CF geometry is discarded from further analyses and attention is focused on the CFC and CCF(C) configurations.

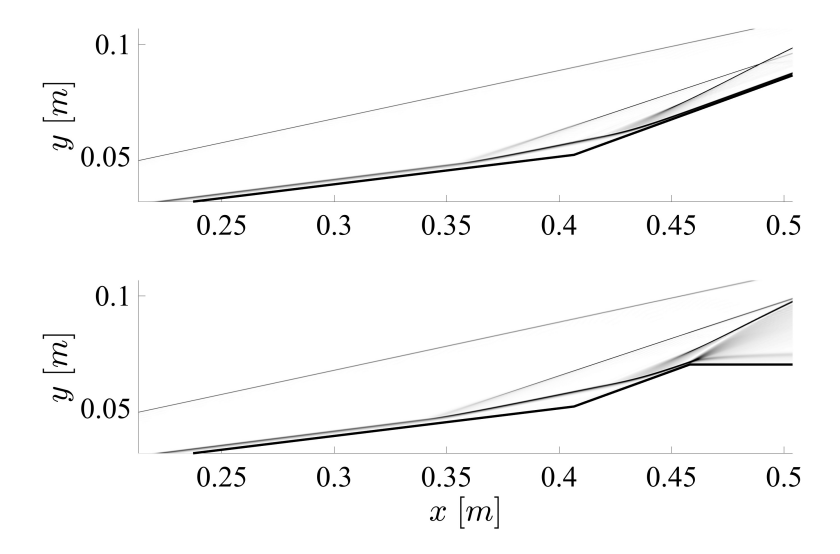


Fig 3. Numerical Schlieren of axisymmetric CF (upper image) and CFC (lower image) flows at $M_{\infty}=6, Re=5\times10^5$, highlighting the vicinity of the flare in the respective geometries

2.4. Conical Flows

In what follows it is instructive to compare linear stability of steady base flow profiles extracted from axisymmetric simulations along the cone surface against those generated by application of the Taylor-Maccoll conical flow approximation to obtain boundary layer edge values, followed by classic compressible conical boundary layer theory [13]. For consistency, Sutherland viscosity law has been used for all results obtained and the local Reynolds number is calculated using the streamwise coordinate of the projection of a point along the cone surface, as schematically shown in Figure 4.

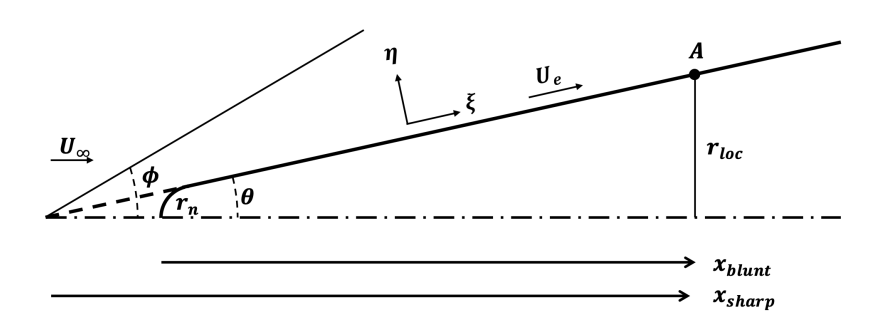


Fig 4. Schematic of the conical flow.

Boundary layer profiles on the conical forebody of the HIFiRE-1 and the ROTEX-T vehicles are extracted at the locations S1–S4 shown in Fig. 1 and are compared against the compressible boundary layer (cBL) profiles computed at the same locations. While the profiles themselves are practically identical, from a linear stability analysis point of view it is essential to monitor the generalized inflection point function, [13]

$$\frac{d}{d\eta} \left(\bar{\rho} \frac{d\bar{u}_{\xi}}{d\eta} \right), \tag{1}$$

and identify its zeros along the local wall-normal direction. To enable such comparisons, the DNS data is smoothed in a three-step procedure. First, the extracted DNS profiles are interpolated onto a higher resolution grid, on which the function $\bar{\rho} \frac{d\bar{u}_{\xi}}{d\eta}$ is calculated. Second, a moving average filter is used to

produce an improved curve on which a third and final Gaussian filter eliminates potentially introduced spurious inflection points and delivers a profile which can be differentiated to form the function shown in Eq. 1.

Generalized Inflection Point (GIP) functions computed by boundary layer theory and extracted from the simulation results are shown in Figure 5. At a glance, one notices the very good near-wall agreement of the two sets of results at S1 (ROTEX-T) and S2 (HIFiRE-1 and ROTEX-T). Interestingly, as the expansion shoulder and the compression corner are approached on the HIFiRE-1 and the ROTEX-T, respectively, the DNS results deviate from those of the boundary layer theory in the expected manner: the numerical simulations deliver a stronger attached profile in the former vehicle and one that is increasingly affected by the proximity to the separation bubble on the latter vehicle.

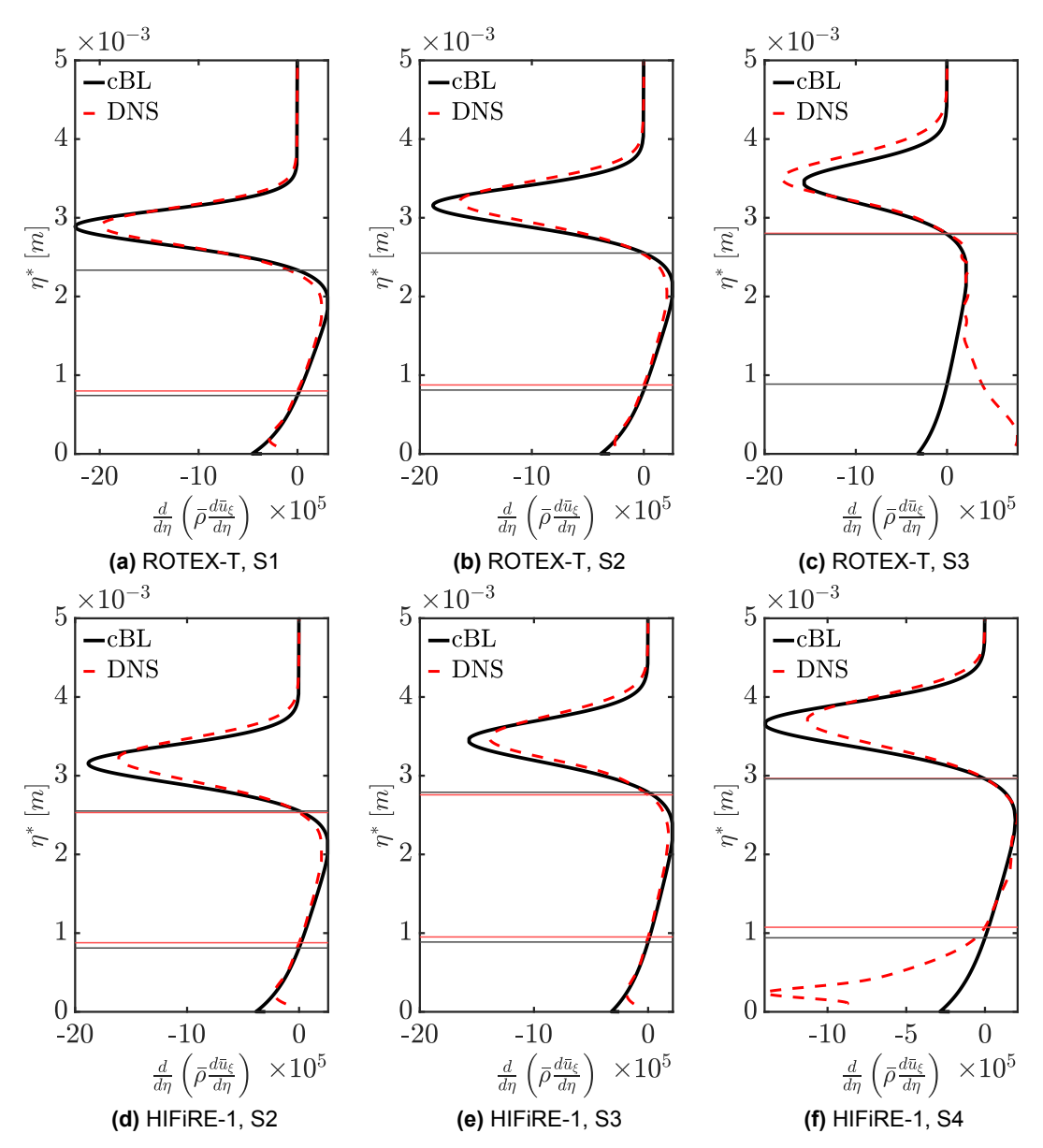


Fig 5. Comparison of GIP functions on the ROTEX-T (upper row, locations S1, S2 and S3) and HIFiRE-1 (lower row, locations S2, S3 and S4) conical forebodies against results of compressible boundary layer theory at $Re = 0.5 \times 10^6$.

3. Linear Stability Analyses

3.1. Local LST analyses on the cone

Figure 6 presents eigenvalue spectra obtained at locations S1–S4 on the respective cones of the ROTEXT and HIFiRE-1 vehicles, at Re=500k and a single frequency, F=136 kHz. A scan of relevant frequencies has been performed, although its results are not shown here for brevity, since all spectra on both vehicles at this and all frequencies examined at this Reynolds number comprise damped eigenmodes. This finding justifies use of modal global stability analysis at the cone-cylinder expansion corner on the HIFiRE-1 and at the flares of both vehicles, in conjunction with homogeneous Dirichlet boundary conditions at the inflow domain, to study self-excited perturbations arising from shock / boundary layer interaction and laminar separation bubble instability at the respective flare locations, in isolation from potentially incoming flow perturbations. As the Reynolds number increases, the present local analyses on the conical forebodies are repeated in a systematic manner, to identify thresholds at which amplified Mack modes may exist on the conical forebody and enter the expansion/compression zones on the two vehicles. In that situation modal global analysis is no longer permissible and alternative analysis approaches are called for.

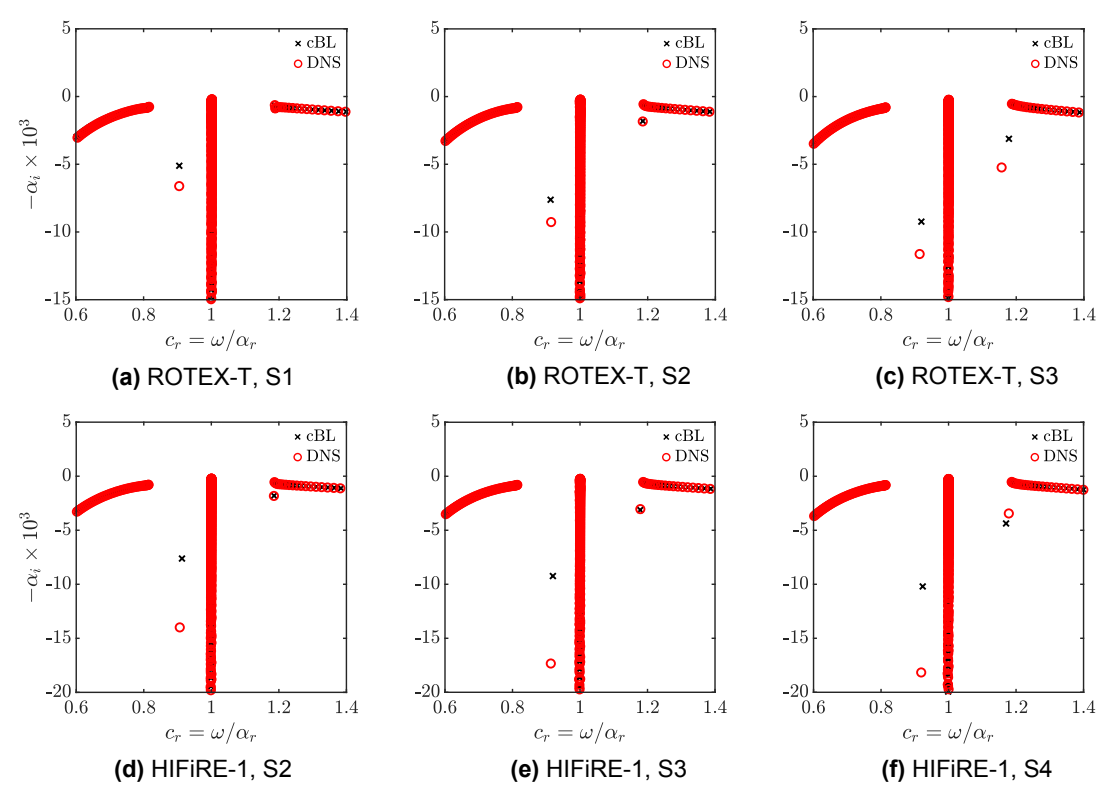


Fig 6. Eigenvalue spectra on the two vehicles at $Re=0.5\times10^6$, at locations S1, S2, S3 and S4 shown on Fig. 1

3.2. BiGlobal Stability

The spatially inhomogeneous regions on the two vehicles mandate use of BiGlobal stability analysis to study the growth of three-dimensional (non-axisymmetric) linear perturbations. Unsteady fields, q, satisfying the full equations of motion are linearized via decomposition into unsteady 3D perturbations $\tilde{q}(x,y,z,t)$ superposed upon the steady basic flow $\bar{q}(x,y)$ as

$$\mathbf{q}(x, y, z, t) = \bar{\mathbf{q}}(x, y) + \tilde{\mathbf{q}}(x, y, z, t)$$
(2)

where $|\tilde{q}| \ll |\bar{q}|$. Omitting quadratic disturbance terms and subtracting the O(1) base flow terms, themselves satisfying the steady equations of motion, results in the linearized Navier-Stokes equations (LNSE). Inserting the BiGlobal ansatz

$$\tilde{\boldsymbol{q}}(x,y,z,t) = \hat{\boldsymbol{q}}(x,y) e^{i(\beta z - \omega t)} + \text{c. c.}$$
 (3)

into the LNSE then allows to turn the initial value problem into a generalized complex non-symmetric eigenvalue problem

$$L\hat{q} = \omega M\hat{q}. \tag{4}$$

In a temporal analysis content the spanwise wavenumber β is then taken to be real and is related to the spanwise wavelength by $\lambda=2\pi/\beta$. In the case of axisymmetric geometries, β is related to azimuthal wavenumber m by

$$\lambda = 2\pi r_{\rm loc}/m$$
,

with $r_{\rm loc}$ defined in Fig. 4. The eigenvalue consists of real and imaginary parts $\omega=\omega_r+i\omega_i$, where ω_r corresponds to the eigenmode frequency and ω_i to its growth rate and flow is considered stable when $\omega_i<0$. Spatial discretization of the eigenvalue problem is accomplished using a newly developed multi-domain method, which permits decomposition of complex domains into quadrilateral subdomains featuring curved boundaries and using independent mappings and resolutions in each subdomain. As such, the present multi-domain method overcomes the restriction of decomposition into rectilinear subdomains [14] and introduces the ability to use non-conformal meshes on curved interfaces. The EVP problem is solved in all subdomains with continuity in function and continuity in the normal-to-interface derivatives of up to n-1 order of the problem being solved. Using the justification provided in the Section $\ref{totaleq}$, homogeneous Dirichlet boundary conditions are applied to the perturbations at the inflow and the wall on all perturbation components except perturbation density, on which homogeneous Neumann conditions are applied. The same Neumann condition is used on all perturbations in the far-field boundary, while the outflow domain is treated by linear extrapolation. The eigenvalue problem is then iteratively solved using the Arnoldi algorithm with Krylov subspace sizes $m_{\rm Kryl}>300$.

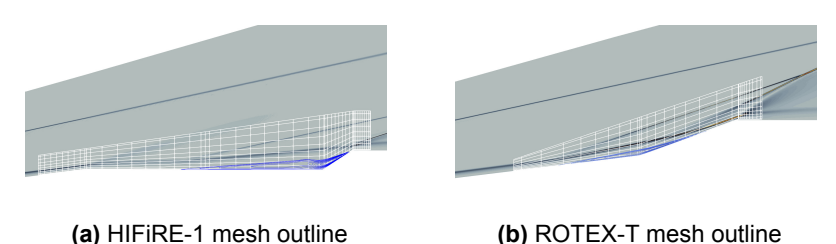


Fig 7. Outline of mesh structure on the HIFiRE-1 (left column) and ROTEX-T (right column)

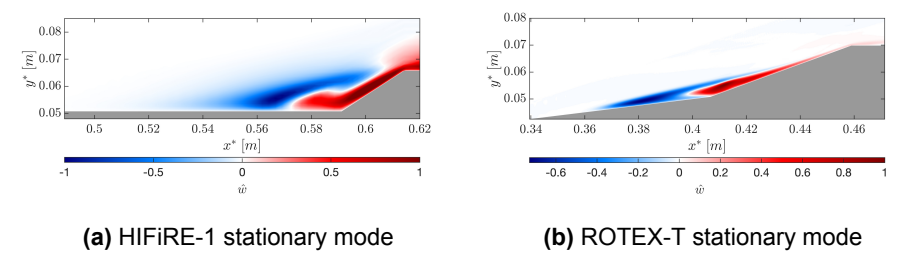


Fig 8. Representative stationary amplitude functions of the azimuthal velocity perturbation on the HIFiRE-1 (left column) and ROTEX-T (right column) at $Re = 0.5 \times 10^6$, m = 3

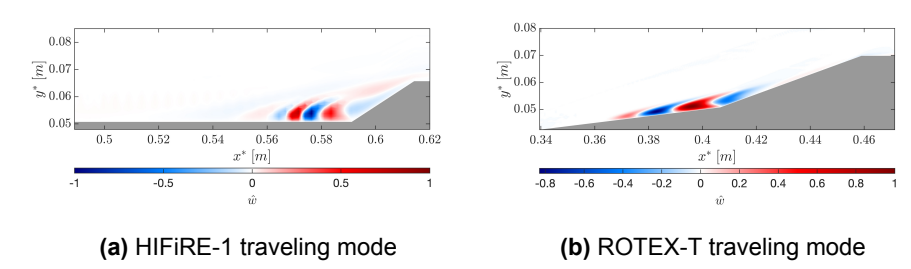


Fig 9. Representative traveling amplitude functions of the azimuthal velocity perturbation on the HIFiRE-1 (left column) and ROTEX-T (right column) at $Re = 0.5 \times 10^6$, m = 3

4. Axisymmetric Direct Numerical Simulations

Direct numerical simulations for the axisymmetric ROTEX-T configuration were conducted in the range of $500 \times 10^3 \le Re \le 2000 \times 10^3$ to identify the onset of global instability and the expected breaking of the laminar separation bubble. Fig. 10 shows the time convergence of the residual of density measured at several probes distributed in the boundary layer along the cone, flare and cylinder section of the vehicle. The respective locations of the probes are shown in the top part of the figure, with the separation bubble identified with a red line. Probe 20, located just inside the reversed flow region of the LSB shows linear decay of the residual with nearly the same slope at all Re. Probe 22, located exactly in the compression corner converges at a slower rate. Probe 25, located at the expansion corner shows linear decal non unlike probe 20, with the slope decreasing with increasing Reynolds number. Probe 26 is located in the cylinder boundary layer downstream of the expansion, where the flow is accelerated. Fast decay of the residual is seen at this location. The slope however, also decreases with increasing Reynolds number suggesting that the boundary layer may eventually become unsteady on the cylinder. In all the probes, some original peaks of the residual can be observed at early times, with the magnitude of the peak increasing proportionally to the Reynolds number. These may be associated with transient growth mechanisms and warrant an a non-modal stability analysis in the future.

The damping rate, ω_i , of the decaying least damped mode can be estimated by computing the slope

$$\omega_i = \frac{\ln(\rho(t_2)/\rho(t_1))}{t_2 - t_1} \tag{5}$$

of the residual in the linear decay regime [15]. Fig. 11 shows the effect of Reynolds number on damping rate at different probes across the separation region (see Fig. 10). The slope for all probes in the figure was measured by doing a linear fit to the residual signal between times of 2×10^{-3} and 2.5×10^{-3} . It can be seen that the rate, with which the damping rate increases with Re grows from probe 20 to 22, i.e. from the separation to the compression corner. After the compression corner, at for probes 23 to 25 located on the flare, the rate of increase of ω_i with Re reduces again. At the compression corner (at probe 22), it grows until Re of about 1500×10^3 and then decays. The eventual decay at higher Reynolds numbers may be misleading, as the bubble has already broken down, as will be shown later on. However, the fact that the highest rate of decrease of the damping rate is seen at the compression corner points to a growth of instability at that location.

The properties of the flow at the wall are plotted in Fig. 12 across the cone-flare-cylinder junction. The locations of the compression and expansion corners are marked with vertical dashed lines. The pressure coefficient increases in the separation bubble and along the flare before dropping down at the expansion. The skin friction coefficient (C_f) , surface pressure coefficient (C_p) and the Stanton number (St) are defined as

$$C_f = \frac{\tau_w}{\frac{1}{2}\rho_{\infty}u_{\infty}^2} \quad C_p = \frac{p_w}{\frac{1}{2}\rho_{\infty}u_{\infty}^2} \quad St = \frac{q_w}{\rho_{\infty}u_{\infty}c_p(T_0 - T_w)},$$
 (6)

where τ_w , q_w are wall shear stress and wall heat flux, respectively. The zero crossing C_f denote the separation and reattachment locations. The primary separation location moves upstream, while the

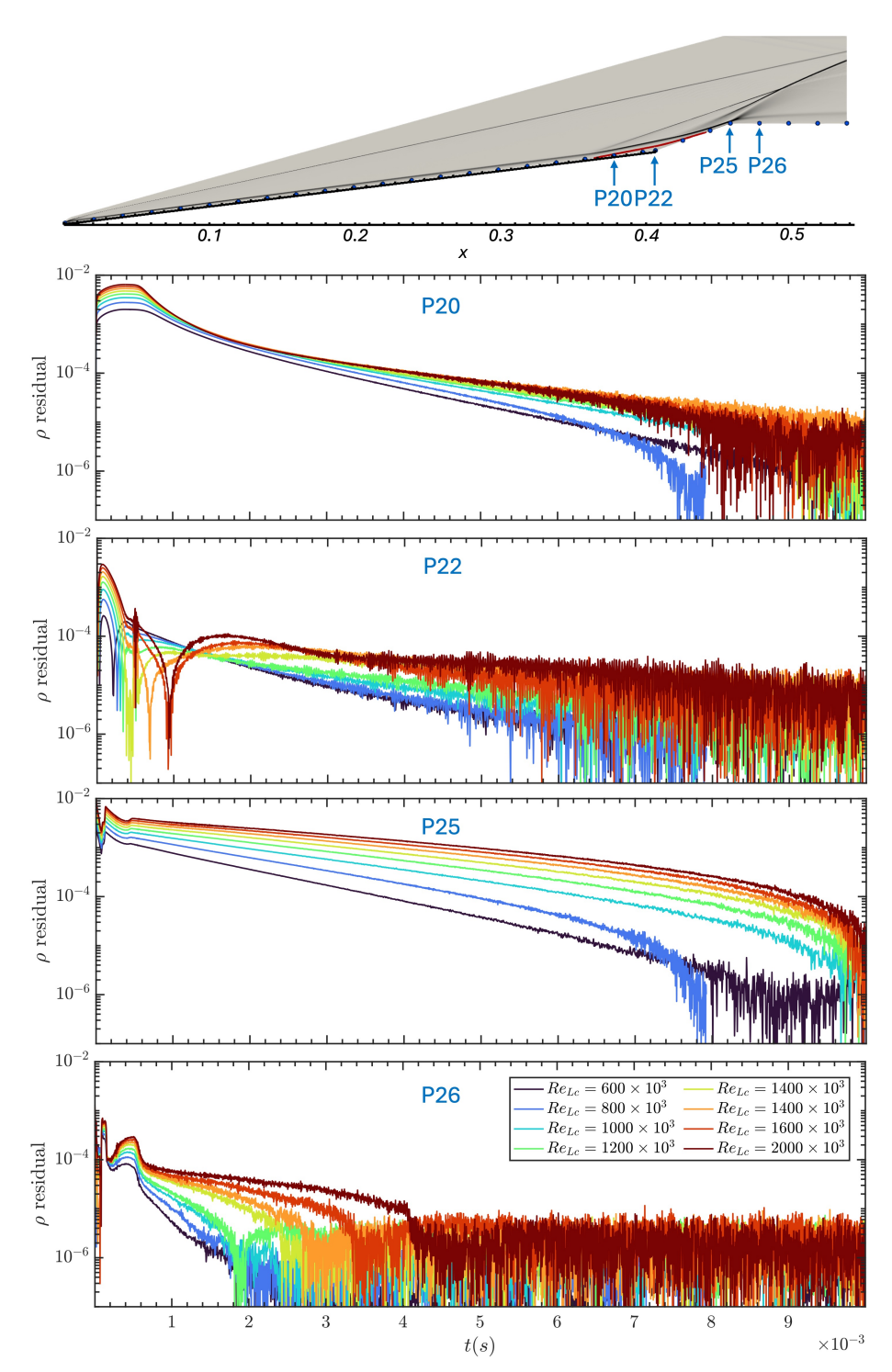


Fig 10. Effect of Reynolds number on the convergence of the density residual at different locations along the cone flare.

primary reattachment moves downstream with increasing Re as the bubble is growing. The inset clearly shows that a breaking of the LSB takes place somewhere $1000 \times 10^3 \le Re \le 1200 \times 10^3$ in the vicinity of the compression corner. This is the same location that showed the highest rate of decrease of the

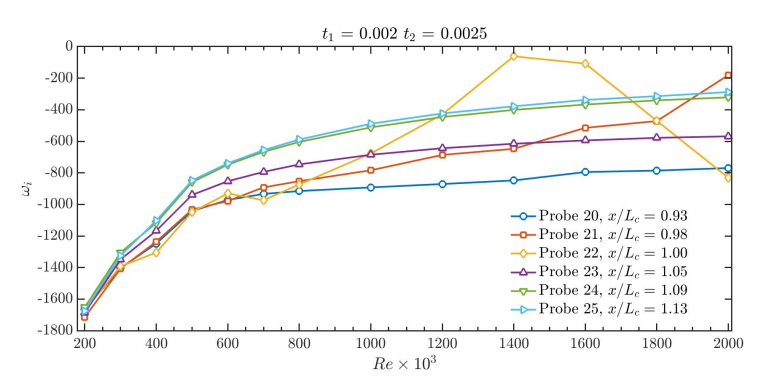


Fig 11. Effect of Reynolds number on damping rate of the density residual measured at different probes across the separation region.

damping rate, The Stanton number profiles show waviness in this region, suggesting that the flow may be unsteady. Similarly, at highest Reynolds numbers, oscillations appear in the profiles along the cone, suggesting that the flow is becoming unsteady there.

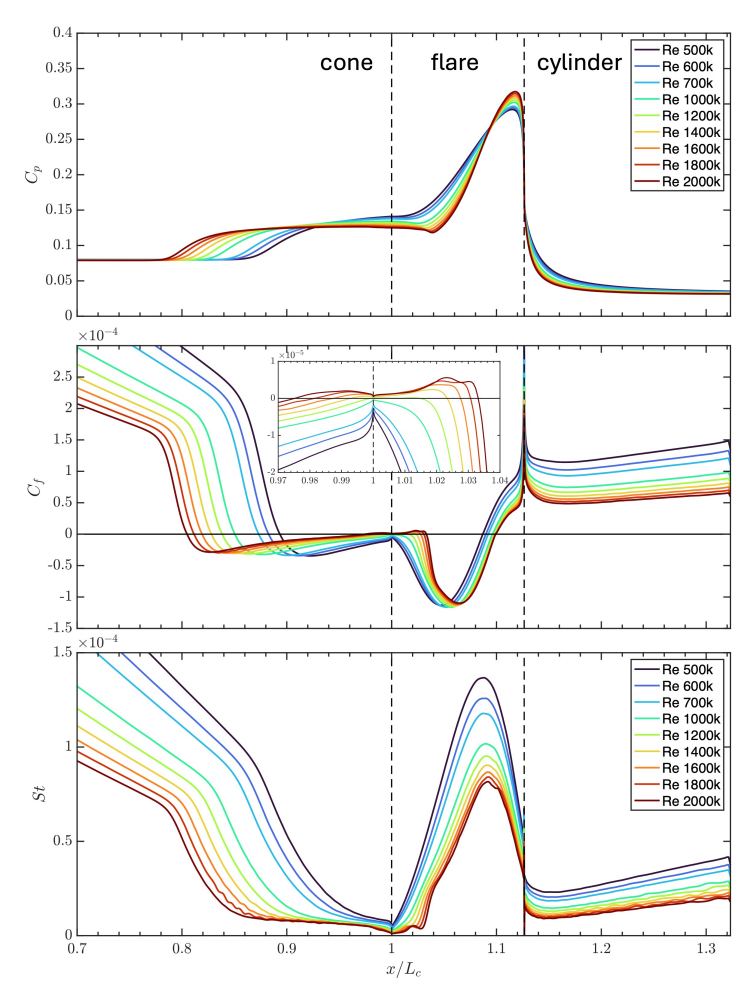


Fig 12. Variation of pressure coefficient, skin friction coefficient and Stanton number along the separated region with Reynold number based on cone length.

4.1. Axisymmetric least damped modes

The spatial structures of the least damped global mode are extracted by post-processing the flow fields at 2×10^{-3} and 2.5×10^{-3} [15] in. The temperature, pressure and vertical velocity components of the resulting perturbations are plotted in Fig. **??** with Re. Temperature, pressure and vertical velocity have structures in the separation and reattachment shocks and temperature and vertical velocity also have structures in the shear layer of the bubble. This is due to the separation and reattachment locations and the corresponding shocks still moving as the flow is converging. However, at $Re \ge 1200\times 10^3$, when the bubble eventually breaks, there are additional modes structures indicating unsteadiness in the bubble near the compression corner. A close up of these structures at $Re = 1800\times 10^3$ is shown in Fig. 13.

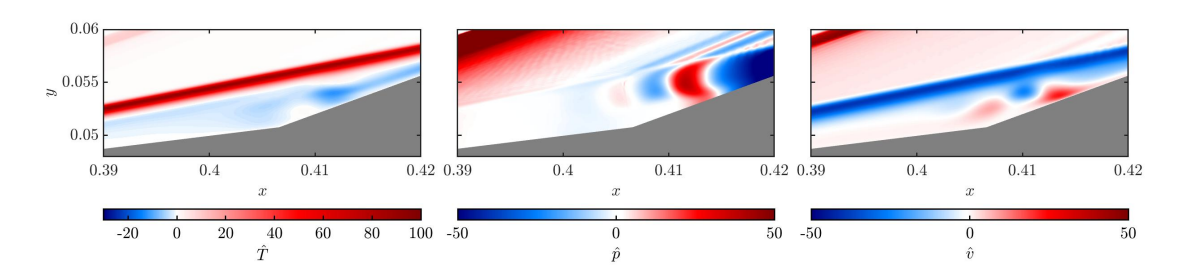


Fig 13. Close up of the least damped mode ar $Re = 1.8 \times 10^6$.

5. Three-Dimensional Direct Numerical Simulations

Finally, we conduct three-dimensional DNS for a quarter at $Re=500\times10^3$. For the quarter setup, symmetric as opposed to periodic conditions are imposed the sides. In addition, a simulation of the full ROTEX-T is performed at $Re=500\times10^3$ to verify if the quarter is sufficient to capture the three-dimensionality. It can be seen that the separation bubble is broken along the azimuthal direction with pockets of higher reversed flow extending periodically from the flare region upstream and that the reattachment line unsteady. Comparison of Fig. 14 and $\ref{eq:condition}$, shows that the quarter ROTEX-T setup captures the spanwise periodicity of the bubble. These three-dimensional simulations show that the separation bubble is broken along the azimuthal direction already at $Re=500\times10^3$, which is far earlier than the two-dimensional breakdown seen at $Re=1200\times10^3$ in the antisymmetric case.

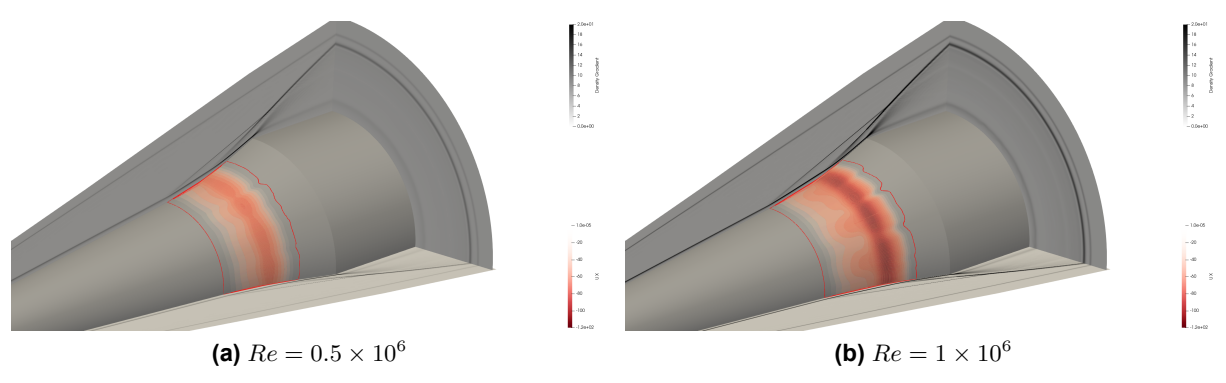


Fig 14. Three-dimensional simulation of the one quarter of the ROTEX-T at $M_{\infty}=6$. Synthetic Schlieren (magnitude of the density gradient) show the structures of the shocks and contours of the reversed flow (in orange) show the separation bubble. Red lines denote separation and reattachment.

Acknowledgments

Work supported by the Air Force Office of Scientific Research under Grant number FA8655-23-1-7031, "Linear modal and nonmodal instability analyses of high-speed laminar separated flow over complex geometries. Part II: The HIFIRE-1, ROTEX-T and Oberkampf vehicles" with Dr. Douglas R. Smith and Dr. Amanda Chou as Program Officers.

References

John D Schmisseur. Hypersonics into the 21st century: A perspective on afosr-sponsored research in aerothermodynamics. *Progress in Aerospace Sciences*, 72:3–16, 2015.

Roger Kimmel and David Adamczak. HIFiRE-1 background and lessons learned. In 50th AIAA Aerospace Sciences Meeting including the New Horizons Forum and Aerospace Exposition, page 1088, 2012.

Thomas Thiele, Ali Gülhan, and Herbert Olivier. Instrumentation and aerothermal postflight analysis of the rocket technology flight experiment rotex-t. *Journal of Spacecraft and Rockets*, 55(5):1050–1073, 2018.

Matthew P Borg, David W Adamczak, Adam J Culler, and Michael D Kurtz. Hiflier hypersonic flight experiment: Design, analysis, and ground test. In *AIAA SCITECH 2025 Forum*, page 0733, 2025.

Jonathan Davami, Thomas J. Juliano, Anton Scholten, Pedro Paredes, Elizabeth K. Benitez, Carson L. Running, Kamil Dylewicz, Vojtech Pezlar, Vassilios Theofilis, Thomas Thiele, and Sebastian Willems. Separation and Transition on the ROTEX-T Cone-Flare. In *AIAA SCITECH 2024 Forum*, pages 1–37. American Institute of Aeronautics and Astronautics, jan 2024. doi: 10.2514/6.2024-0499.

Jonathan Davami, Thomas J Juliano, Nolan Little, Lian Duan, Christopher Ostoich, Eric Blades, Zachary B Riley, Elizabeth K Benitez, Matthew P Borg, and S Michael Spottswood. Effect of surface deformation on hypersonic transitional shock-wave/boundary-layer interactions on the rotex-t cone-flare. In *AIAA SCITECH 2025 Forum*, page 1307, 2025.

Thomas J Juliano, David Adamczak, and Roger L Kimmel. HIFiRE-5 flight test results. *Journal of Spacecraft and Rockets*, 52(3):650–663, 2015.

Thomas J Juliano, Matthew P Borg, and Steven P Schneider. Quiet tunnel measurements of HIFiRE-5 boundary-layer transition. *AIAA Journal*, 53(4):832–846, 2015.

Meelan Choudhari, Chau-Lyan Chang, Thomas Jentink, Fei Li, Karen Berger, Graham Candler, and Roger Kimmel. Transition analysis for the HIFiRE-5 vehicle. In *39th AIAA Fluid Dynamics Conference*, page 4056, 2009.

Pedro Paredes, Ryan Gosse, Vassilis Theofilis, and Roger Kimmel. Linear modal instabilities of hypersonic flow over an elliptic cone. *Journal of Fluid Mechanics*, 804:442–466, 2016.

Helio Quintanilha Jr, Pedro Paredes, Ardeshir Hanifi, and Vassilis Theofilis. Transient growth analysis of hypersonic flow over an elliptic cone. *Journal of Fluid Mechanics*, 935:A40, 2022.

Ryan Gosse, Roger Kimmel, and Heath Johnson. CFD study of the HIFiRE-5 flight experiment. In *40th Fluid Dynamics Conference and Exhibit*, page 4854, 2010.

Lester Lees and Chia Chiao Lin. Investigation of the Stability of the Laminar Boundary Layer in a Compressible Fluid, September 1946.

J. de Vicente, J. Basley, F. Meseguer-Garrido, J. Soria, and V. Theofilis. Three-dimensional instabilities over a rectangular open cavity: from linear stability analysis to experimentation. *Journal of Fluid Mechanics*, 748:189–220, 2014.

V Theofilis. On steady-state flow solutions and their nonparallel global linear instability. *Advances in turbulence VIII*, pages 35–38, 2000.